Front. Optoelectron. 2016, 9(2): 206–224
DOI 10.1007/s12200-016-0631-2

REVIEW ARTICLE

Review of design principles of 2D photonic crystal microcavity biosensors in silicon and their applications

Swapnajit CHAKRAVARTY (✉)[1*], Xiangning CHEN[2,3*], Naimei TANG[2], Wei-Cheng LAI[2], Yi ZOU[2], Hai YAN[2], Ray T. CHEN (✉)[1,2]

1 Omega Optics Inc., Austin, TX, 78757, USA
2 Department of Electrical and Computer Engineering, University of Texas at Austin, Austin, TX, 78712, USA
3 School of Electronic Science and Engineering, Nanjing University, Nanjing 210093, China

Abstract In this paper, we reviewed the design principles of two-dimensional (2D) silicon photonic crystal microcavity (PCM) biosensors coupled to photonic crystal waveguides (PCWs). Microcavity radiation loss is controlled by engineered the cavity mode volume. Coupling loss into the waveguide is controlled by adjusting the position of the microcavity from the waveguide. We also investigated the dependence of analyte overlap integral (also called fill fraction) of the resonant mode as well as the effect of group index of the coupling waveguide at the resonant wavelength of the microcavity. In addition to the cavity properties, absorbance of the sensing medium or analyte together with the affinity constant of the probe and target biomarkers involved in the biochemical reaction also limits the minimum detection limits. We summarized our results in applications in cancer biomarker detection, heavy metal sensing and therapeutic drug monitoring.

Keywords photonic crystal (PC) sensor, biosensor, slow light, photonic crystal microcavity (PCM), photonic crystal waveguide (PCW), high sensitivity, high specificity, photonic integrated circuits (PICs), nanophotonics

1 Introduction

It is generally accepted that while the twentieth century is the era of microelectronics, optoelectronics and photonics spurred by the advent microlithography, integrated circuits, the free-space ruby laser and semiconductor chip-integrated lasers, the twenty-first century is expected to be an era where electronics and photonics start to play a dominant role in the field of healthcare. Better medical facilities accompanied by longer average lifespan ensure that the demand for new technologies promising better diagnostic, and accompanying therapeutic capabilities, will continue to flourish. The invention of the laser in the twentieth century led to the progress of optical lithography. As silicon became the platform of choice of the semiconductor industry, Moore's law led to increased device miniaturization. Large room-size Electronic Numerical Integrator And Calculator (ENIAC) computers started to shrink to mobile blackberries and IPads with significantly larger computational processing capabilities. The silicon electronics revolution ignited the imaginations of people toward a plethora of applications on smaller and smaller mobile platforms that has enabled better connectivity and a faster life.

Photonics, offers several advantages over electronics, particularly the freedom from electromagnetic interference, the faster speed of light compared to electrons, and of course, the absence of charging and discharging effects of electrons, when photons interact with biologic fluids thereby facilitating the studies on the basic cellular building blocks in water based media in the field of medicine. Various techniques like enzyme linked immune-absorbent assays (ELISA) [1], Western Blot [2], Northern Blot [3], etc. to name a few made use of free-space visible lasers for optical diagnostics and till date, these methods form the basic diagnostic tools in clinics worldwide. A common thread among all techniques for qualitative and quantitative diagnostics is the use of molecular labels [1–4] that are excited by light. Surface plasmon resonance (SPR) devices enabled the first label-free optical sensors [5], thereby enabling the optical detection of a reaction between a probe and target biomarker without the steric

Received February 22, 2016; accepted February 29, 2016

E-mail: swapnajit.chakravarty@omegaoptics.com, raychen@uts.cc.utexas.edu

---

[*] Joint first author

hindrance of detection labels. Over the last decade, silicon photonics based label-free sensors have made increasing headway, employing the primary device platforms of strip waveguides [6], Mach-Zehnder interferometers [7], gratings [8], ring resonators [9] and photonic crystal (PC) [10–12] devices. The miniaturization afforded by silicon photonics promises the capability of transitioning bench-top optical diagnostics to a mobile, portable, hand-held platform [13,14]. Sensor adaptors that interface with smartphones have been demonstrated with grating based surface normal coupled devices [13]. However, the minimum detection limits in surface normal detection systems are at significantly larger concentrations than those demonstrated in the ring resonator and in our instance, the two-dimensional (2D) PC sensor platform, wherein the sensing mechanism employs integrated optics on a silicon chip for light guiding and signal transduction. In this paper, we review our research with silicon 2D PC sensors comprising 2D photonic crystal microcavities (PCMs) coupled to 2D photonic crystal waveguides (PCWs) and their applications in cancer research and drug diagnostics. We review the totality of design aspects that must be considered in the design of 2D PC sensors in silicon.

PCs are periodic dielectric structures with a periodic variation in the dielectric constant that gives rise to photonic pass and stop bands similar to electronic bandgaps in semiconductors. Point defects and line defects in a periodic structure give rise to microcavities and waveguides respectively, wherein the light is trapped and confined in the PCM, or is confined and propagating in a PCW. Since 3D PCs are difficult to fabricate using conventional planar lithography techniques, much work over the past two decades has focused on 2D PCs wherein the confinement in-plane is provided by the 2D PC, and out-of-plane by total internal reflection (TIR). Silicon has been the chosen material for PCs for passive photonic integrated circuits (PICs) while for active PICs with lasers and detectors, III-V materials such as GaAs and InP have been used. Our work in silicon 2D PCs was done in the 1.55 μm telecom wavelength band to make use of numerous optical sources and detectors that are easily available in this wavelength, to enable the development of low-cost sensors.

Various designs of PCMs have been proposed for chemical [15] and bio-sensing [16] using microcavities with small mode volumes. Radiation losses, however, increase with increasing refractive index of the ambient that significantly reduces the resonance quality (Q) factor due to reduced out-of-plane confinement in 2D PCs. Thus, although high Q-factors have been demonstrated in freely suspended PC membranes in air [17], which promises the potential for highly sensitive sensing in air, when such membranes are suspended in phosphate buffered saline (PBS) (refractive index n = 1.334), a typical ambient for bio-molecules, the Q-factors deteriorate by orders of magnitude. Hence researchers have attempted optimum designs balancing two contradictory requirements: increasing the Q-factor of the resonance versus increasing the wavelength shift due to change in refractive index. In passive silicon PC nanostructures, the transmission drop-resonance architecture has been used predominantly with hexagonal [16] and linear PCM coupled to a W1 PCW.

2 A typical device and measurement principle

The PCW is typically a hexagonal structure with a W1 line defect waveguide with uniform lattice constant a = 400 nm, where W1 denotes that width of the PCW is $\sqrt{3}a$. Silicon slab thickness and air hole diameter are $h = 0.58a$ and $d = 0.54a$ as shown in Fig. 1(a). A microscope image of a typical patterned device with an array of two PCM resonators is shown in Fig. 1(b). We consider single PCM sensors only. In Fig. 1(a), we note that by an ink-jet patterning, the minimum ink-jet dispensed spot size of biomolecules is ~35 μm. The ink-jet dispensed spot size determines the minimum spacing between adjacent sensors, and is different from the device surface area that can be functionalized by combining lithographic patterning with ink-jet printing [18]. PCMs of gradually increasing length were thus investigated to characterize resonance line-widths and sensitivity.

Linear PCMs L_n, where n presents the number of missing holes along Γ–K direction, are fabricated two periods away from the PCW. The edge air holes are shifted in the Γ–K direction by 0.15a [19]. Figure 1(c) shows a simulated band structure obtained by three-dimensional plane-wave expansion simulations of the W1 PCW, considering water (n = 1.33) as the ambient. The normalized resonant mode frequencies of different PCMs of increasing lengths obtained by 3D finite-difference time domain (FDTD) simulations are indicated by dotted lines in Fig. 1(c). The resonant mode profiles are shown in the inset.

Light is guided in and out of the PCW by ridge waveguides with PC group index taper to enable high coupling efficiency into the slow light guided mode [20]. Devices were fabricated on silicon-on-insulator (SOI) wafer using established methods [20]. The bottom cladding of silicon dioxide (n = 1.46) is kept intact to enable robust devices with high yield. Devices were tested with transverse electric (TE)-polarized light by end-fire coupling method with polarization maintaining single mode tapered lensed fibers. The transmission drop resonance Q and sensitivity to bulk refractive index changes are analyzed with water and isopropyl alcohol (IPA) (n = 1.377) as the ambient medium. Figures 2(a) – 2(c) show experimental transmission spectra from W1 PCWs with coupled L3, L7 and L13 PCMs in water. In Figs. 2(d) – 2(f), drop transmission of the resonance closest to the band edge, as in insets of Fig. 1(b), for L3, L7 and

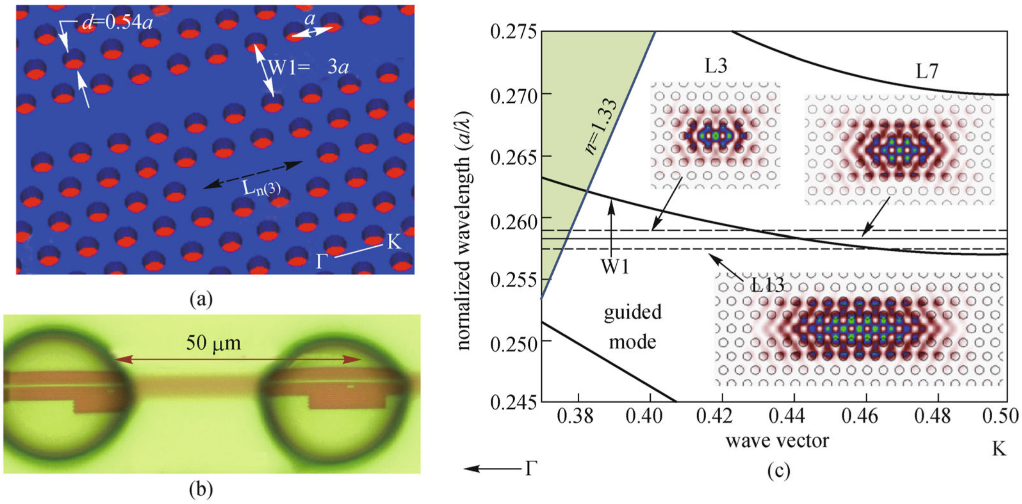

Fig. 1 (a) Device schematic; (b) ink-jet printed biomolecules on PC devices showing spacing between printed spots (scale bar is 10 μm); (c) dispersion diagram of W1 PCW in water. The W1 guided mode is shown together with frequencies of resonant modes for L3, L7 and L13 PCMs by dashed lines. Respective mode profiles are shown in insets [21]

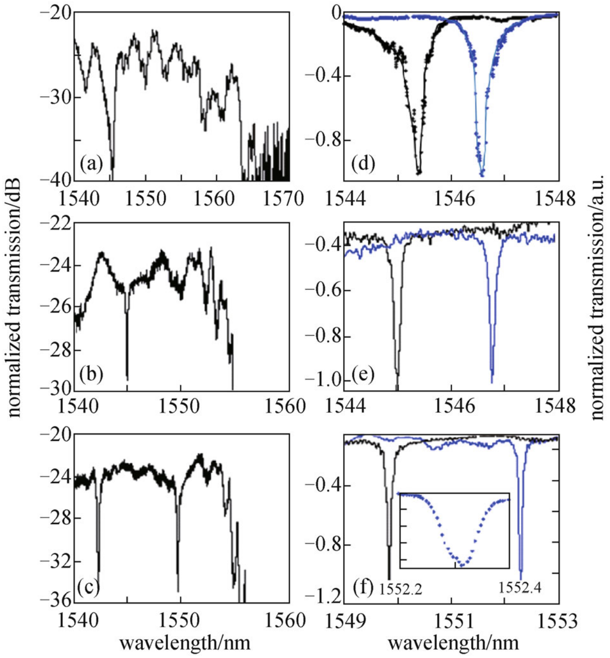

Fig. 2 Experimental W1 PCW transmission spectrum in water with coupled (a) L3, (b) L7 and (c) L13 microcavities. Experimental spectra showing shift of resonance mode closest to the band edge in (a), (b) and (c) in (d), (e) and (f) respectively in water (black) versus IPA (blue). Inset (e) magnifies the wavelength range [21]

L13 PC microcavities in water and IPA are shown.

Figure 3 shows resonance shifts $\Delta\lambda$ observed experimentally with the device in water versus in IPA. Figure 3 also plots experimental Q (= $\lambda/\Delta\lambda$) in water and IPA, at the center frequency, and the approximate resonance offset $\Delta\Lambda$ from the W1 transmission band edge. It is observed from Fig. 3 that as the resonance moves closer to the band edge of the W1 PCW, Q and $\Delta\lambda$ increase. Since IPA does not absorb in the wavelength range studied, Q in IPA is higher than in water.

3 Analysis of the design principles

The resonance shifts $\Delta\lambda$ determine the concentration of the analyte being tested. In subsequent sections, we describe the detailed design work to maximize the sensitivity and minimum detection limits of 2D PC structures in sensing applications.

3.1 Controlling the cavity radiation loss out-of-plane

The total quality factor Q_{T} of the resonance mode of an isolated PCM, which is related to the photon lifetime τ_{p}, at frequency ω by $Q_{\mathrm{T}} = \omega\tau_{\mathrm{p}}$ is given by

$$\frac{1}{Q_{\mathrm{T}}} = \frac{1}{Q_{\mathrm{R}}} + \frac{1}{Q_{\mathrm{i}}}, \tag{1}$$

where $Q_{\mathrm{R}} = \omega\tau_{\mathrm{R}}$ and $Q_{\mathrm{i}} = \omega\tau_{\mathrm{i}}$, τ_{R} and τ_{i} represent the radiation loss and intrinsic cavity loss respectively. τ_{R} is given by

$$\frac{1}{\tau_{\mathrm{R}}} = \frac{P_{\mathrm{R}}}{W_{\mathrm{E}}}, \tag{2}$$

where P_{R} denotes the total power radiated by the cavity and W_{E} denotes the stored energy in the cavity which is proportional to the cavity mode volume. Hence a method that reduces P_{R} and increases W_{E} will decrease the

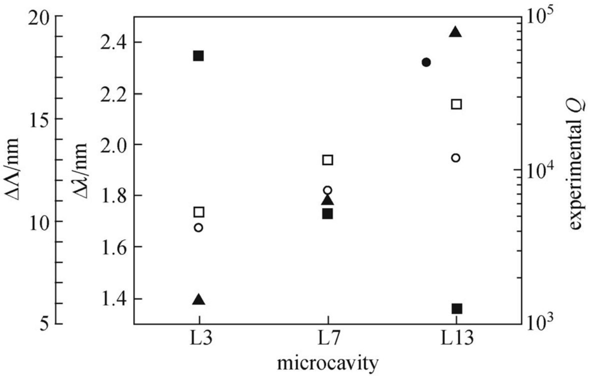

Fig. 3 Plots showing trends in L3, L7 and L13 PCMs for resonant mode (a) quality factor Q in water (open circle), (b) quality factor Q in IPA (open square), (c) approximate mode offset from the transmission band edge (filled square, left offset axis) and (d) wavelength shift from water to IPA (filled triangle, left axis) [21]

radiation loss from the cavity and hence increase the effective Q. A high Q implies that the light is trapped for a longer period of time in the cavity and hence interacts longer with any analyte in the vicinity of the PCM. In addition, since W_E is proportional to the optical mode volume, a higher W_E leads to the potential for larger optical mode overlap with the analyte which also contributes to higher sensitivity.

The frequency of the resonance mode is indicated by the black dashed line in the dispersion diagram of the W1 PCW by 3D plane-wave expansion (PWE) in Fig. 1(c). The dispersion diagram of the W1 PCW is shown by the solid black curves.

The higher Q in L13 PCMs is due to the combined effects of lower radiation loss as the resonance moves deeper into the photonic band gap compared to L3 PCMs [21,22] that are studied conventionally, and the larger mode volume of L13 PCMs compared to L3 PCMs. Higher Q thus increases the ability to detect small changes in concentration. Furthermore, the increased length enables larger overlap of the optical mode with the analyte leading to higher sensitivity. It must be noted here, that in the geometry selected here, the loss from the microcavity into the PCW also contributes a term Q_{WG} to Eq. (1) [23].

3.2 Controlling the cavity loss into adjacent waveguide for light coupling

The total quality factor Q_T of the resonance mode of a PCM side coupled to a PCW is thus given by

$$\frac{1}{Q_T}=\frac{1}{Q_i}+\frac{1}{Q_R}+\frac{1}{Q_{WG}}, \tag{3}$$

where $Q_{WG} = \omega\tau_{WG}$, and τ_{WG} represent time constant for waveguide loss. Since 35 μm is the dispensed spot size, we consider designs with gradually increasing PCM length to take advantage of Eq. (1), but also taking into consideration the new term in Eq. (3). Similar to Fig. 2, the simulated dispersion diagram of a W1 PCW is shown in Fig. 4(b). The resonance frequencies of the L13 and L21 PCMs are shown by the dotted black and dotted red lines respectively. As the cavity size increases from L13 to L21, the resonance frequency moves closer to the band edge and P_R decreases. Since W_E is larger for the L21 PCM, Q_R is effectively increased. As observed from Fig. 4(b), the group index of the W1 PCW at the coupling frequencies is higher for the L21 (n_g = 16) compared to the L13 (n_g = 13.2) PCM. Enhanced optical coupling from the waveguide to the microcavity leads to enhanced light-matter interaction thus improving sensitivity as we have shown elsewhere [24].

In an uncoupled cavity, increasing the length of the PCM increases the total Q of resonance modes. However, simply increasing the length of the microcavity from L13 to L21 based on Eq. (2) does not increase Q_T for the resonance modes of interest in the cavity-waveguide architecture. A longer cavity leads to increased leakage from the cavity to the PCW leading to lower Q_{WG} which lowers the effective Q_T. A high Q_T is desirable since it enables smaller changes in concentration to be detected. Hence, an optimum design requires optimizing the cavity-waveguide coupling for high Q and high sensitivity, in addition to other factors such as the magnitude of slow light in the coupling waveguide that we will discuss later [24]. To optimize Q_T while enhancing sensitivity, the PCM is moved laterally away from the PCW to increase Q_{WG}. Since Q_{WG} is primarily determined by the number of periods between the PCM and the PCW, we fabricated devices in which the L21 PCM is located 2, 3, 4 and 5 rows away from the PCW. Figure 5 shows the experimental Q (= $\lambda/\Delta\lambda$).

As the L21 PCM moves away from the PCW, Q increases indicating reduced cavity to waveguide loss and improved optical confinement by the PCM. At the same time, the normalized frequency of the resonance mode increases as the dielectric fraction in the vicinity of the PCM decreases as it moves away from the PCW. From the dispersion diagram in Fig. 4(b), a higher normalized

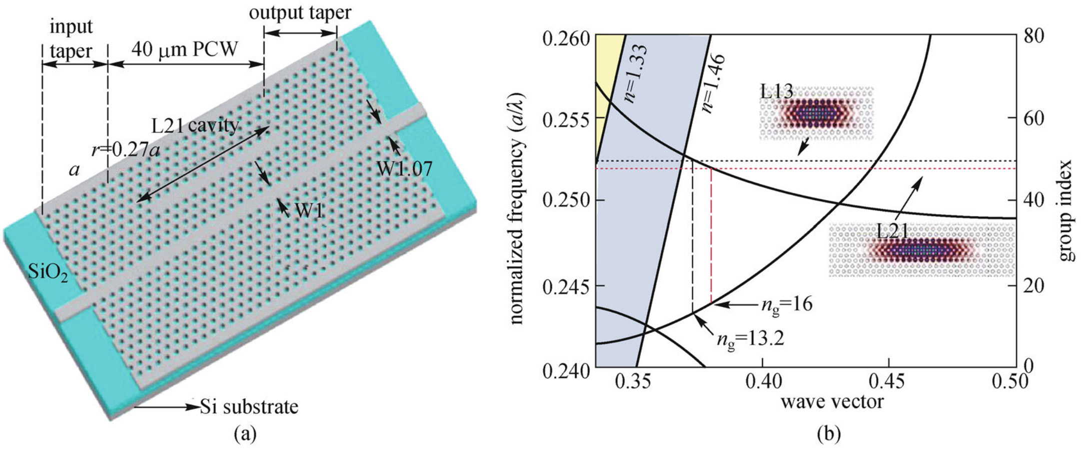

Fig. 4 (a) Schematic of PCM device; (b) dispersion diagram of W1 PCW inwater. The W1 guided mode is shown together with frequencies of resonant modes for L13 and L21 PCMs by black and red dashed lines respectively. The mode profiles are shown in insets [23]

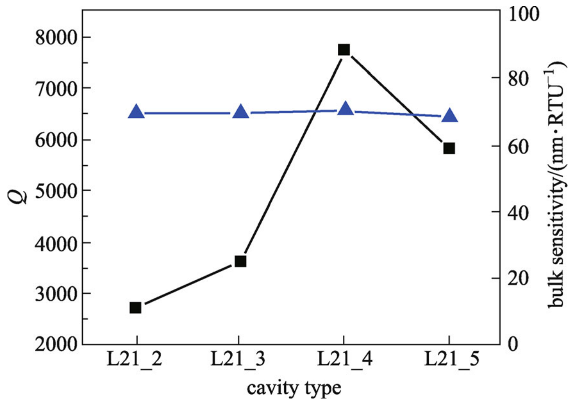

Fig. 5 Q-factors (black squares) and bulk sensitivity (blue triangles) variation of L21 microcavity side coupled to W1 PCW in water versus microcavity location change (L21_2 represents L21 microcavity 2 rows away from the PCW) [23]

frequency implies more radiation loss as a greater fraction of the optical mode is above the light line, which will decrease Q_R. Q_i will also decrease as the PCM moves further away from the W1 PCW due to the increased mode overlap with surface roughness of more surrounding holes.

A limiting situation is reached when the PCM is located more than 4 rows away from the PCW.The increase of Q_R and Q_i dominate over the increase in Q_{WG} and hence the effective Q_T decreases. Since the loss rate from the cavity to the waveguide and vice-versa is directly proportional to the cavity length, the highest Qs will be achieved at different distance of the cavities from the PCW for cavities of different lengths such as L13 and L21. The L13 PCMs in Fig. 1 were considered 2 rows away laterally from the W1 PCW. For our L21 PCM, it is observed in Fig. 5, that when the PCM is located 4 rows away from the PCW, Q reaches a maximum. The Q of a L21 PCM located 2 rows away from the W1 PCW (Q~2500) is lower than the Q of a L13 PCM located 2 rows away from the W1 PCW. Hence, a simple increase of the cavity length does not increase Q; other factors such as the cavity-waveguide coupling determined by Q_{WG} need to be engineered. The bulk sensitivities of the L21 PCM devices shown in Fig. 5, change negligibly as the L21 PCM is moved away from the W1 PCW, since the mode volume of the microcavity changes negligibly as the cavity is moved farther away from the W1 PCW.

In general, Q_{WG} is primarily determined by the distance, in terms of number of periods, of the PCM from the PCW as well as the orientation of the PCM with respect to the PCW. It is obvious that Q_T will increase with increasing distance of the PCM from the W1 PCW; however, since the coupling efficiency between the PCW and the PCM decreases with increasing distance of the PCM from the PCW, further work is in progress to determine the optimum separation of the PCM from the PCW for sensing applications.

3.3 Controlling the analyte overlap integral of the resonant cavity mode

Resonator based sensors are characterized by a resonance that shifts in frequency or wavelength in response to a change in the ambient refractive index (for bulk sensing) or a change in the refractive index caused by biomolecules in the vicinity of the surface of the resonator (for biosensing). The response can be understood by first order perturbation theory [25], in which the change in eigenfrequency $\Delta\omega_m$ of the mth mode can be described as

$$\Delta\varpi_m = \frac{\varpi_m}{2}\frac{\langle \boldsymbol{E}_m|\varepsilon_l|\boldsymbol{E}_m\rangle_{V_{\text{liquid}}}}{\langle \boldsymbol{E}_m|\varepsilon_l|\boldsymbol{E}_m\rangle_{V_{\text{liquid+dielectric}}}}\frac{\Delta\varepsilon_l}{\varepsilon_l}\frac{1}{v_{g,m}}, \tag{4}$$

where $\Delta\varepsilon$ is the change in dielectric constant of the analyte from ε_l upon perturbation, and $v_{g,m}$ is the group velocity of the mth mode at the frequency ω_m. Equation (4) implies that the magnitude of wavelength/ frequency shift for a given mode caused by a small index change is directly proportional to the fill fraction f_B, defined as the ratio of electric field energy existing outside of a dielectric structure to the total, and inversely proportional to the group velocity.

$$f_B = \frac{\langle \boldsymbol{E}_m|\varepsilon_l|\boldsymbol{E}_m\rangle_{V_{\text{liquid}}}}{\langle \boldsymbol{E}_m|\varepsilon_l|\boldsymbol{E}_m\rangle_{V_{\text{liquid+dielectric}}}}. \tag{5}$$

In Fig. 6(a), the electric field intensity is simulated by 2D FDTD method for different isolated L_i-type PCMs (i = number of missing holes) and f_B in water is computed. Typically, in silicon 2D PCs, light is coupled from a PCW into an adjacent PCM [10,21–24]. An isolated PCM is considered for simulations in order to eliminate the effect of coupling between the PCM and the PCW in cavity-waveguide coupled sensors [20–24]. Simulations considered water (refractive index RI = 1.33) as the ambient medium and a silicon effective index (n_{eff}) = 2.9 for operation at 1550 nm. The radius of the holes of the bulk PC lattice is ($R = 0.275a$, where a = lattice constant). We note from Fig. 6(a) that f_B for the TE polarized optical mode in water is highest in a L0 cavity (where two adjacent holes in the lattice are shifted by $0.15a$). f_B increases from L3 to L21 PCMs. Commercial ring resonator sensors use TE polarization with thin waveguides for higher analyte overlap integrals to overcome significant bend losses in waveguides with transverse magnetic (TM) polarization [9].

Defect holes are introduced into the L13 PCM at the antinodes of the resonance mode. A scanning electron micrograph (SEM) of the device is shown in Fig. 6(b). Simulated TE-confined electric intensity profile in Fig. 6(c) shows strong optical localization at the defect holes. In PCMs with defect holes, R_D denotes the radius of the defect hole as a fraction of R. While f_B increases in fractions of percentages from L3 to L21, when defect holes are introduced, a dramatic increase by 8% in f_B is observed. The resonance mode closest to the PCW transmission band edge is considered [20–24]. We consider defect holes > 90 nm diameter for better fabrication tolerance and yield in high volume manufacturing. We refer to such low-index defects as defect holes, rather than nanoholes elsewhere. Such devices have been fabricated by 193 nm immersion lithography [27].

Devices are fabricated on a SOI wafer in 250 nm silicon on a 3 μm bottom oxide cladding, which offers better structural stability than free standing membranes. The air hole radius is R = 108 nm. Figure 7(a) shows PCW transmission spectrum in water with $R_D = 0.6R$. Defect holes raise the frequency of the resonance mode in the photonic band gap. Consequently, the width of the PCW is reduced for efficient coupling to the PCM at the slow light guiding wavelengths.

The optimized waveguide width indicated in Fig. 7(a) is W0.855 where W0.855 denotes that the width of the PCW is $0.855 \times \sqrt{3}a$. To determine sensitivity in refractive index unit (RIU), measurements are done in water (RI = 1.33) and glycerol (RI = 1.45). The bulk sensitivity increased by 66% from ~68 nm/RIU for L13 [21] to ~112 nm/RIU for the L13 PCM with defect holes for different R_D as shown

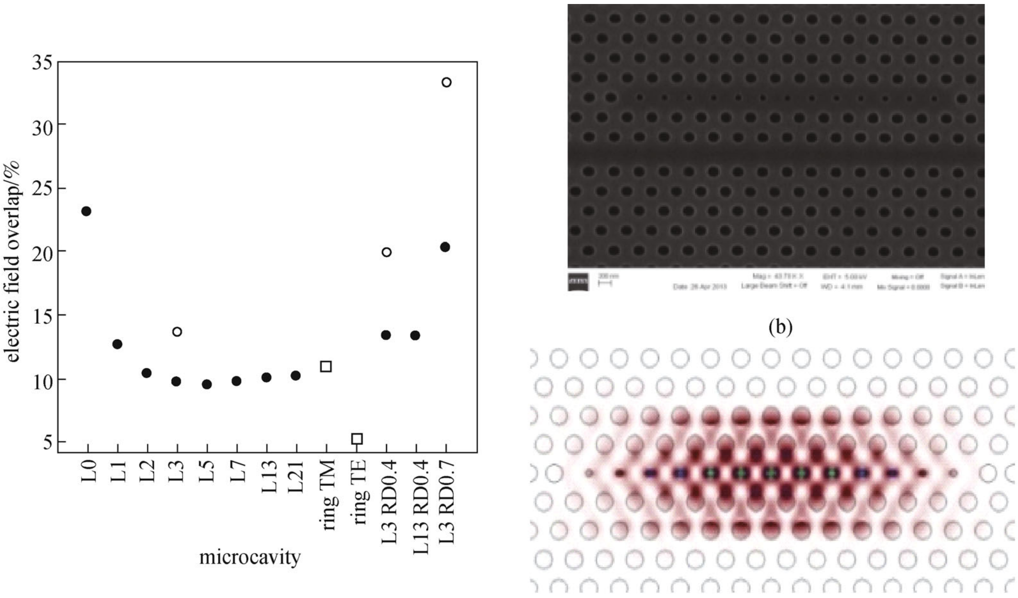

(a)

(b)

(c)

Fig. 6 (a) 2D FDTD simulated fill fraction/field overlap computed for different PCMs with $R = 0.275a$ (filled circles), $R = 0.35a$ (open circles) and ring resonator (open square). Ring TM value is taken from Ref. [9] for a ring resonator with diameter 30 μm and width 500 nm; (b) SEM image of L13 PCM with defect holes; (c) mode profile of the confined defect mode in (b) [26]

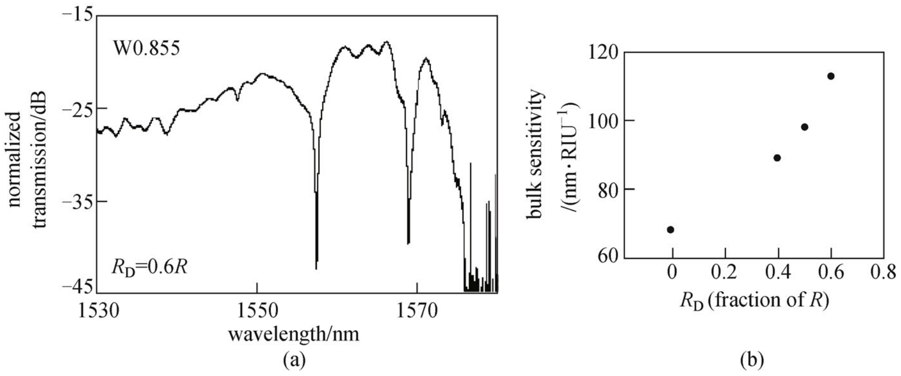

Fig. 7 (a) Transmission spectra for PCWs in water with $R_D = 0.6R$; (b) bulk sensitivity computed from experimentally observed resonance wavelength shift from water to glycerol for different R_D [26]

in Fig. 7(b). The experimentally observed Q is between 1×10^4 and 1.5×10^4. When $R = 0.35a$, $R_D = 0.7R$, the calculated f_B is 32%; a sensitivity of 200 nm/RIU can thus be expected by linear extrapolation [16].

3.4 Effect of analyte absorbance

Equations (4) and (5) clearly indicate that sensitivity of a sensor for bulk sensing can be increased by increasing f_B, so that detection limit (DL) is inversely related to sensitivity (S). However, a critical parameter in computing DL is the intrinsic quality factor (Q_i) of the resonator and the total Q due to analyte absorbance. We estimate the DL for water at (λ_m = 1550 nm) (absorbance α~800 m^{-1}). We also consider a hypothetical liquid with RI = 1.33 having absorbance 0.1 m^{-1} at 1550 nm. The total Q is calculated as [28]

$$\frac{1}{Q} = \frac{1}{Q_i} + \frac{1}{Q_R} + \frac{1}{Q_{WG}} + \frac{1}{Q_\alpha}, \tag{6}$$

$$Q_\alpha = \frac{2\pi n}{\lambda_m f_B \alpha}, \tag{7}$$

where, we now add the new term, Q_α which is the quality factor due to optical absorption at wavelength λ_m, α is the analyte absorbance, and n is the refractive index weighted by f_B. n is calculated as $n = f_B n_A + (1 - f_B) n_S$, where n_A and n_S are refractive indices of analyte and dielectric respectively.

The Ln-type PC cavity can be considered as a closed PCW. Consequently, at the resonance frequency, group index n_g of the mode can be considered the same as in an open ended PCM (or equivalently a PCW). Taking into account the effect of slow light and f_B enhancement on absorbance by a factor γ [25,29], Eq. (7) can now be written as

$$Q_\alpha = \frac{k}{\alpha} = \frac{2\pi n}{\lambda_m f_B \alpha} \frac{n_{eff}}{n_g}, \tag{8}$$

$$\gamma = f_B \frac{c}{n_{eff}} \frac{1}{v_{g,m}}, \tag{9}$$

where k is the wavevector and n_{eff} is the mode effective index with no slow light effect. In a L21 PCM [23], n_g~16.

Assuming a signal to noise ratio (SNR) of 60 dB, with no other sources of noise, the standard deviation of linewidth ($\Delta\lambda_{FWHM}$) is given by [29]

$$\sigma \approx \frac{\Delta\lambda_{FWHM}}{4.5(\mathrm{SNR}^{0.25})}. \tag{10}$$

The DL is calculated as [28]

$$\mathrm{DL} = \frac{3\sigma}{S}, \tag{11}$$

where

$$S = \frac{\lambda_m}{n_{eff}} f_B n_g. \tag{12}$$

3.5 Summarizing the effective minimum detection limit for biosensing

The minimum detectable concentration (C_{min}) is dependent on Q, n_g and f_i. From Ref. [28], the resonance wavelength shift ($\delta\lambda$) is proportional to the sensitivity (S) and biomolecule surface density (σ_p). From Eq. (9), $\delta\lambda$ can be expressed as [28]

$$\delta\lambda \propto \lambda \sigma_p f_i n_g, \tag{13}$$

C_{min} is proportional to the bulk DL, and related inversely to f_i and n_g. Equation (13) does not account for the size of the detection area or affinity constant between a probe and its conjugate biomolecule.

Bio sensing was conducted with biotin as probe receptor and avidin as target protein [20–24]. Figure 8 plots $\delta\lambda$ versus concentration for four different PCMs, L13, L21, L55, and L13 with defect hole. When $R_D = 0.4R$, the lowest concentration detected is 1 fM (67 fg/mL),

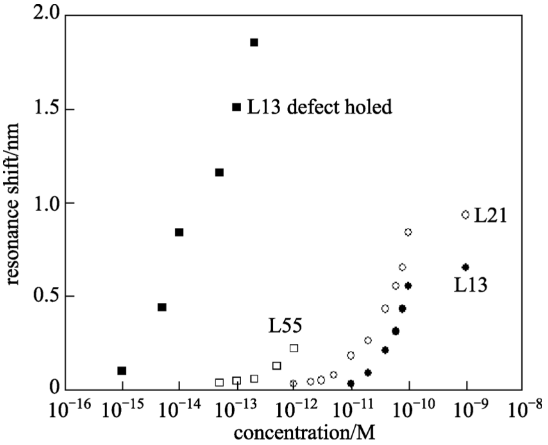

Fig. 8 Bio sensing spectral shifts ($\delta\lambda$) in L13, L21, L55 and L13 defect holed PCMs. 1 M = 1 mol/L [26]

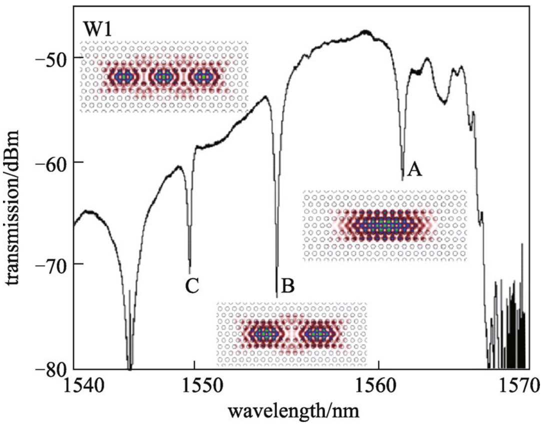

Fig. 9 Experimental transmission spectrum, showing the resonance modes and mode profiles in the insets [24]

compared to 10 pM in L13 cavity [22] without defect holes.

The resonance mode frequency offset from the band edge is closest in L55 PCM followed by L21 and L13. Since n_g increases with decreasing wavelength offset from the W1 PCW transmission band edge, a larger $\delta\lambda$ is observed in L55 with higher (n_g ~20) than in L21 ($n_g = 16$) [23] and L13 (n_g = 13) PCMs [21] for a given concentration as seen in Fig. 8. In addition to a larger optical mode volume, the larger $\delta\lambda$ in L55 PCMs therefore enhances the ability to detect lower concentrations, within the limitations set by measurement apparatus. Larger n_g in PCMs thus also results in larger $\delta\lambda$ and higher sensitivity when compared to ring resonators.

From Eq. (13), based on n_g ~20, the 22 μm long L55 PCM is apparently 5 times more sensitive in biosensing than ring resonators. In the L55 PCM, $\delta\lambda$ = 50 pm at the minimum detected concentration of 3.35 pg/mL with avidin (67 kDa). The 30 μm diameter ring resonator detected a minimum 3.3 pg/mL of streptavidin (55 kDa); however $\delta\lambda$ = 0.1 pm [9] which is 500 times smaller $\delta\lambda$ than the L55 PCM, although binding affinities in both cases is same (dissociation constant K_d~10^{-15} M) [30].

The larger f_i (due to larger f_B) for the L13 PCM with defect holes results in a larger $\delta\lambda$ compared to the L13 PCM without defect holes. Equation (13) and f_B data in Fig. 6(a) suggests a factor of 1.25 enhancement, however experimental data shows 4 orders of magnitude enhancement in minimum concentration detected in biosensing. Empirical data therefore suggests a superlinear relation between f_i and $\delta\lambda$ and hence the minimum experimentally detected concentration.

3.6 Effect of group velocity in the coupling waveguide on sensitivity

Figure 9 shows that multiple resonances of the L13 PCM are dropped from the transmission spectrum of the W1 PCW. We limit our study to the three modes labeled A, B and C nearest to the W1 PCW transmission band edge. Figure 10 plots the dispersion diagram that shows the resonance mode of the L13 PCM coupled to the W1 PCW. The resonance mode frequencies of A, B and C are calculated from the experimental transmission spectrum in Fig. 9. The band edge in Fig. 9 corresponds approximately to $a/\lambda = 0.25$ where the simulated group index is $n_g = 33$ as seen from Fig. 10(a). The experimental band edge is offset from the simulated band edge due to high transmission losses at higher n_g values and is consistent with maximum n_g ~35 observed experimentally in air-clad PCW structures [31]. It is observed that at the coupling frequencies of modes A, B and C, the group velocities of the W1 PCW guided mode are 13.2, 9.8 and 7.9, respectively.

Devices were measured in water (refractive index n = 1.33) and glycerol (n = 1.46) and the bulk sensitivity in nm/RIU was determined and plotted in Fig. 10(b) for the individual modes A, B and C. Figure 10(b) shows that mode A has the highest bulk sensitivity of 66 nm/RIU. Figure 10(b) also plots the Q and the bulk sensitivities of modes A, B and C when the L13 PCM is coupled to wider PCWs W1.025 and W1.05 (W1.05 indicates that the width of the PCW is $1.05 \times \sqrt{3}a$, where a is the lattice constant of the PC pattern). Figure 11 plots the sensitivity of the respective modes A, B and C as a function of concentration of the biomolecule avidin, which binds to its conjugate specific biotin that is immobilized on the L13 PCM that is coupled to a W1 PCW. It is observed from Fig. 11 that mode A shows the highest sensitivity. The difference in wavelength shifts of the resonance modes is much larger than the 0.02 nm wavelength accuracy of our optical spectrum analyzer.

With respect to the modes A, B and C, it is expected that the sensitivity is determined by the mode Q as well as the optical overlap of the mode with the analyte near the surface of the PCM and the holes in the vicinity of the PCM.

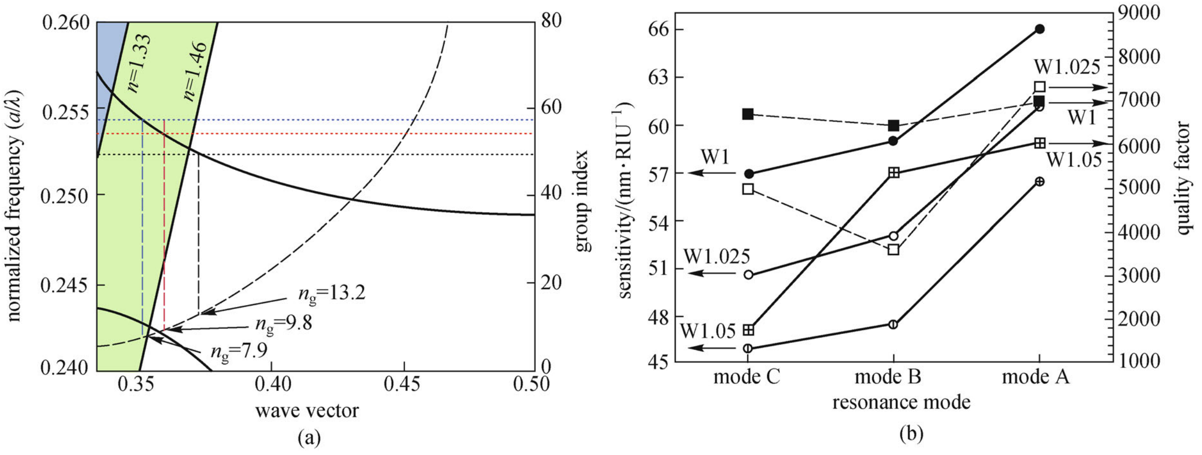

Fig. 10 (a) Dispersion diagram in water of the W1 PCW with the coupled L13 PCM mode frequencies A, B, C shown in black, red, blue dotted lines respectively. Simulated group index of the W1 PCW is shown on the right axis; (b) sensitivity values and Q-factors in water of resonance modes A, B and C are shown for W1 as filled circles and filled squares respectively, for W1.025 as open circles and open squares and for W1.05 as crossed circle and crossed squares respectively [24]

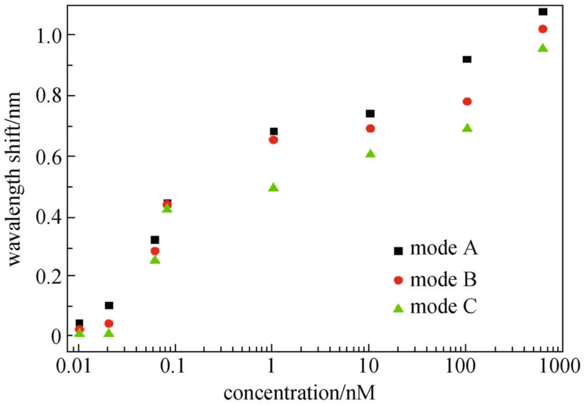

Fig. 11 Wavelength shift of each resonance modes at different concentration. Solid square dots denote the resonance mode A. Solid circle dots denote mode B, and the solid triangle dots are mode C [24]

Q of the modes A and B are nearly the same within the range of experimental variation of Q. The optical overlap of modes A and B, estimated from the mode profile by integrating over an area where the E-field intensity is more than 50% of the maximum value [32] and including the entire internal surface area of the holes along the periphery of the PCM, is nearly the same. However, the optical coupling efficiency from the W1 PCW of resonance mode A is much higher than that of B. The coupling efficiency η between the cavity and the waveguide is described by [24]

$$\eta \propto \frac{1}{v_g}, \tag{14}$$

where v_g denotes the group velocity at the resonance frequency of the corresponding optical mode. v_g is inversely proportional to n_g. Since the coupling strength is inversely proportional to v_g, farther away from the band edge where v_g is high, the coupling strength is low. As a result of the lower optical coupling of incident light into the optical cavity for mode B compared to mode A, light-matter interaction inside the cavity is also reduced which contributes to the lower sensitivity of B compared to A. Similarly, resonance modes A, B and C have decreasing sensitivity in order, when the L13 PCM is coupled to the wider PCWs W1.025 and W1.05.

3.7 Biochemistry aspect: effect of dissociation/association constants on sensitivity

Wafers were functionalized by treating with 10% by volume 3-aminopropyl-triethoxy-silane (3-APTES) in toluene. It is then washed 3 times in toluene to remove unbound 3-APTES, 3 times in methanol to remove toluene and finally 3 times in de-ionized water to remove methanol. The wafers are then incubated in 1% glutaraldehyde in PBS for 5 min and washed 3 times in PBS and ink-jet printed with target antibodies in glycerol. Past research has shown that the 3-APTES-glutaraldehyde coupled layer retains its initial activity for several weeks [33]. Hence we do not expect any reduction in activity within the 30 min by which time the target antibodies are printed. The printed spots were left to incubate overnight. Subsequently, all target antibodies not bound to the functionalized device layer were removed by washing 3 times in PBS. After overnight incubation and washing, the device is coated with bovine serum albumin (BSA) to prevent any non-specific binding and washed 3 times with PBS. The device is now ready for measurements.

Before a new addition of probe antibody solution, the resonance wavelength was measured (λ_1). For each concentration of newly added probe antibody solution, the chip was incubated in the probe antibody solution and the resonance wavelength monitored as a function of time. No resonance wavelength shift was observed for 20 min. After 20 min, the resonance wavelength increased as a function of time, until the shift saturated after another 20 min at λ_2. The chip was next washed 3 times in PBS to remove unbound probe antibodies and the resonance wavelength λ_3 ($< \lambda_2$) measured again. The final resonance wavelength shift $\Delta\lambda$, is plotted later, given by $\Delta\lambda = \lambda_3 - \lambda_1$.

The binding between a target antibody and its conjugate probe antigen/antibody is governed by the three equilibrium equations below. The nomenclature that is followed is that target refers to the receptor biomolecule that is linked to the silicon substrate while probe refers to the biomolecule in the sample solution that will bind specifically to the target if it is the conjugate of the target. Assuming that [P] denotes the concentration of probe biomolecules, [T] denotes the concentration of target antibodies and [PT] denotes the complex formed by the binding of the target biomolecule to the probe biomolecule, the equilibrium equation is given by Ref. [34]

$$\mathrm{P} + \mathrm{T} \leftrightarrow \mathrm{PT}. \tag{15}$$

The factor which determines whether the reaction proceeds more favorably forward or backward is the dissociation constant (K_d) or its reciprocal, the affinity constant (K_a), according to

$$K_\mathrm{d} = \frac{[\mathrm{P}][\mathrm{T}]}{[\mathrm{PT}]} = \frac{1}{K_\mathrm{a}}. \tag{16}$$

K_d is thus a measure to describe the strength of binding (or affinity) between receptors and their ligands. Hence, the amount of probe biomolecules that remain bound to the target biomolecules at any instant of time is larger for a conjugate pair with lower K_d.

The magnitude of binding is determined by de Feijter's formula [35] that relates the absolute amount of adsorbed molecules M per unit surface area with the change in refractive index as

$$M = d_\mathrm{A} \frac{n_\mathrm{A} - n_\mathrm{C}}{\frac{\mathrm{d}n}{\mathrm{d}c}}, \tag{17}$$

where d_A is the thickness of adsorbed layer, n_A is the refractive index of adsorbed molecules, n_C is the refractive index of cover solution (in this case, the probe biomolecule solution), dc represents the differential change in concentration of adsorbed molecules as a function of distance from the silicon surface, and dn is the differential change in refractive index of adsorbed molecules, also a function of distance from the silicon surface, which is proportional to the shift dλ in position of the resonance peak. The magnitude of resonant wavelength shift is proportional to the amount of adsorbed biomolecules and hence provides a label-free means to quantitatively determine biomolecules of interest.

Since K_d determines how many probe biomolecules and hence the amount of bound probe biomolecule mass to the target receptor biomolecules on the silicon surface, from de Feijter's equation, the magnitude of resonant wavelength shift is larger for a conjugate pair with lower K_d. We selected the Table 1 of target receptor antibody and conjugate probe antibodies for our study. Table 1 also lists the corresponding dissociation constants.

The items we acquired are as follows: rabbit anti-goat IgG (Bio-Rad Laboratories, Cat. #: 172-1034), goat anti-rabbit IgG (Bio-Rad Laboratories, Cat. #:170-6515), human IL-10 (Insight Genomics, Cat #: RP027), IL-10-rat anti-human (Invitrogen, Cat #: RHCIL1001), biotin (Sigma, CAS #: 1405-69-2), avidin (Sigma, CAS #: 89889-52-1), bovine serum albumin (Invitrogen, Cat #: 15561-020), 3-APTES (Acros, CAS #:919-30-2), glutaraldehyde (Fischer Scientific, CAS#111-30-8).

The resonant wavelength shift is maximum for the conjugate pair of avidin (67 kDa)-biotin which has the smallest K_d ~10^{-15} M since Eq. (15) shows that the denominator is higher when the exponent in K_d is larger. Both rat anti-human IL-10 and goat anti-rabbit IgG antibodies have a molecular weight of 150 kDa. Yet, since the human IL-10 to rat anti-human IL-10 K_d~10^{-10} M compared to the rabbit anti-goat IgG to goat anti-rabbit IgG binding K_d ~10^{-6} M, hence a larger resonant wavelength shift is observed with rat anti-human IL-10 conjugation biochemistry.

As summarized from results in Fig. 12, the sensitivity of PC biosensor sensitivity is a function of the dissociation constant of the binding reaction. The results also prove the ability of PC biosensors to be used effectively in analyzing binding kinetics.

3.8 Comparing the minimum detection limits of different integrated photonics platforms

Figure 13 summarizes the sensitivities and detection limits demonstrated in PCMs compared to other label-free methods, including SPP devices [5], opto-fluidic ring

Table 1 Target and probe protein conjugates

target protein	probe protein	$K_\mathrm{d}(M)$, dissociation constant
rabbit anti-goat IgG	goat anti-rabbit IgG	~10^{-6} (Kuo et al., 1993) [36]
human IL-10	IL-10, rat anti-human	~$10^{-9} – 10^{-11}$ (de Groote et al., 1994) [37]
biotin	avidin	~10^{-15} (Scullion et al., 2011) [38]

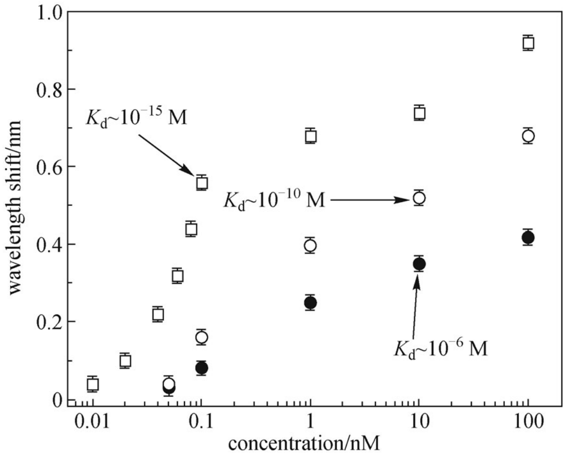

Fig. 12 Resonance wavelength shift of the L13 PCM as a function of concentration for various probe-target conjugates in Table 1 as a function of K_d. Filled circles ●: binding of goat anti-rabbit IgG to rabbit anti-goat IgG (K_d ~10^{-6} M); open circles ○: binding of rat anti-human to human IL-10 (K_d ~10^{-10} M); open squares □: binding of avidin to biotin (K_d~10^{-15} M) [22]

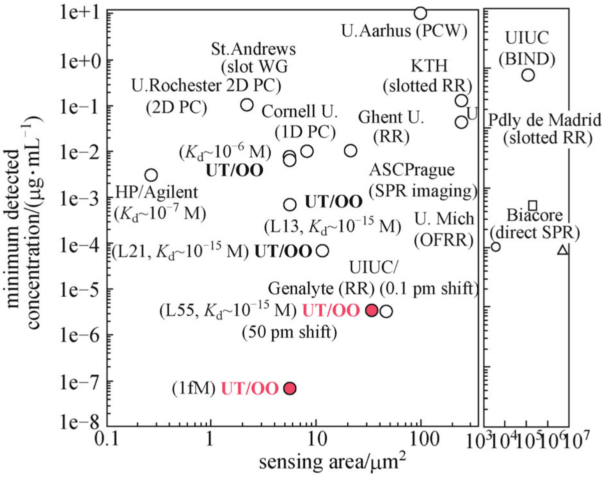

Fig. 13 Chart comparing minimum detection limits of PCM based biosensors versus other label-free optical platforms as a function of sensing area on chip

resonators [39], ring resonator [1,40–42] and other PC devices [10,16,38,43–45], as function of sensing area. The sensitivities as a function of dissociation constant is also reflected in this figure. The PC devices thus demonstrated the highest sensitivities among existing chip-integrated nanophotonic sensing technologies.

4 Dense integration of miniature PCMs: 64 simultaneous sensors

Dense integration of PC sensors on chip for high throughput sensing requires that PCMs be laid out in series and parallel in the optical circuit. We demonstrated that multimode interference (MMI) power splitters can be employed to connect several PCM sensors in parallel [46]. Multiplexing of two and five H1 (one missing or modified hole) PCMs in series were demonstrated previously in 2D [47] and 1D [44] PCs respectively. While the 1D PC couples to a ridge waveguide at group index n_g~3.7, the 2D H1 PCM couples to the 2D PCW at n_g~4.2. 2D PCMs of the L3, L13 or L55 types (where L*n* denotes that the PC microcavity is formed by removing *n* holes along the Γ–Klattice direction in a hexagonal lattice), have demonstrated experimentally higher sensitivities [20–24] than devices in Refs. [44,47]. In L*n* type PCMs, the resonances couple to the PCWs at $n_g > 12$ [20–24]; hence group index engineering is necessary from coupling strip waveguides to the input and output of the PCWs to overcome Fresnel reflection losses at the resonance frequency of the PCM. We experimentally demonstrated that group index taper engineering [48,49] is necessary to efficiently multiplex L3-type PCMs in series. We demonstrated a dense microarray of 64 microcavity-based sensor nodes with series and parallel connected PCM sensors, all sensors being simultaneously interrogated at the same instant of time, from a single optical source.

The engineered PC structure has a L3 PCM side coupled to a W1 line defect PCW, where L3 denotes 3 missing air holes and W1 denotes that the width of the PCW is √3*a* where *a* is the lattice constant. Silicon slab thickness and air hole diameter are h = 250 nm and d = 0.55*a* respectively. For TE polarization, the PCW only supports a single propagation mode inside the bandgap as shown in the dispersion diagram in Fig. 14. The band diagram of the

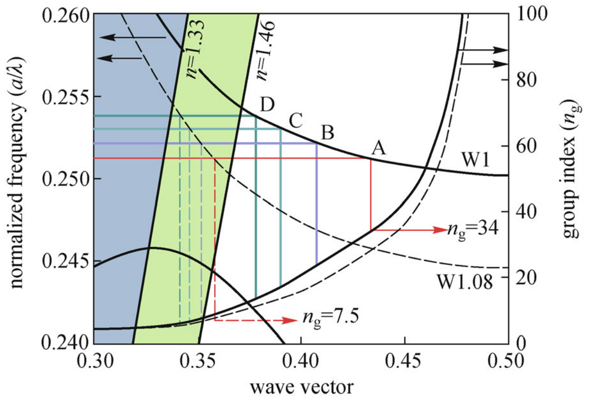

Fig. 14 Schematic of the PC sensor device with input and output strip waveguide, PC tapers, PC guiding region and L3 PCM; (b) dispersion diagrams of W1 (solid), and W1.08 (dash) PCWs in water (n = 1.33) for PC with a = 392.5 nm. The normalized resonance frequency of the coupled PCM at a = 392.5 nm is denoted by D. C, B, and A denote the normalized resonance frequencies of L3 PCMs in PC regions with a = 393.5, 394 and 396 nm respectively cascaded in series with D (a = 392.5 nm). Group index is plotted and its magnitude at the couplingfrequency indicated in respective colors [49]

W1 PCW is obtained by 3D plane wave expansion (PWE) simulations, considering water (refractive index n = 1.33) as the ambient.

Four such structures of L3 PCMs coupled to a W1 PCW, are connected in series to result in 4 PCMs in series, as shown in Fig. 15(b). In contrast to previous designs, where the two PCMs are coupled to the same PCW, the isolated PCM design ensures negligible cross-talk between individual sensors. Each PC structure in series is designed with a different lattice constant a of 392.5, 393.5, 394, and 396 nm respectively to stagger the transmission band edge in each PC section. Since the L3 PCM resonance is offset by a fixed wavelength (~20 nm) from the transmission band edge of the corresponding PCW, the staggering of lattice constants thus ensures that the individual PCM resonances do not overlap in the final output transmission spectrum. In each PC pattern, the group index taper is engineered by gradual widening of the PCW from W1 to W1.08 near the coupling strip waveguide. W1.08 indicates that the width of the PCW in that section is 1.08 × $\sqrt{3}a$. Figure 14 is the dispersion diagram of the W1 PCW with the smallest lattice constant a = 392.5nm. The dispersion profile for the W1.08 PCW, also at a = 392.5 nm, is shown by the dashed black line. The corresponding group indices are also indicated in the figure.

Figure 16 plots the output transmission spectra from 2, 3 and 4 cascaded L3 PCMs in series, with and without index taper. All spectra are measured in water with the objective to implement biosensing.

With group index tapers, as shown in Figs. 16(a) – 16(c), 2, 3, and 4 resonant peaks respectively are clearly seen. In Fig. 16(c), when four PCMs are connected in series as shown in Fig. 16(b), the resonances of the L3 PCMs in the respective sections are dropped from the transmission spectrum of the series connected W1 PCWs. The four resonances are indicated as A, B, C, and D respectively arising from resonances in largest to smallest lattice constant PC sections. The resonances are easily distinguished, and the bandedges are also sharp with 20 dB extinction ratio between the transmission band and the band gap. In contrast, in Figs. 16(d) – 16(f), without PC group index tapers, the resonant peaks are probably buried in noise fringes resulting from group index mismatch between the strip waveguide and PCW.

The normalized resonance frequencies of 4 cascaded L3 PCMs are calculated from the experimental transmission spectrum as indicated by lines with different colors A, B, C and D in Fig. 14. In demarcating the position of the resonance wavelength in the dispersion diagram, based on previous results [24,48], we estimate that the group index at the experimentally observed transmission bandedge is n_g ~35. Mode D represents the microcavity resonance for the L3 PCM in the PC pattern with smallest lattice constant a = 392.5 nm. The resonance wavelength that is dropped by

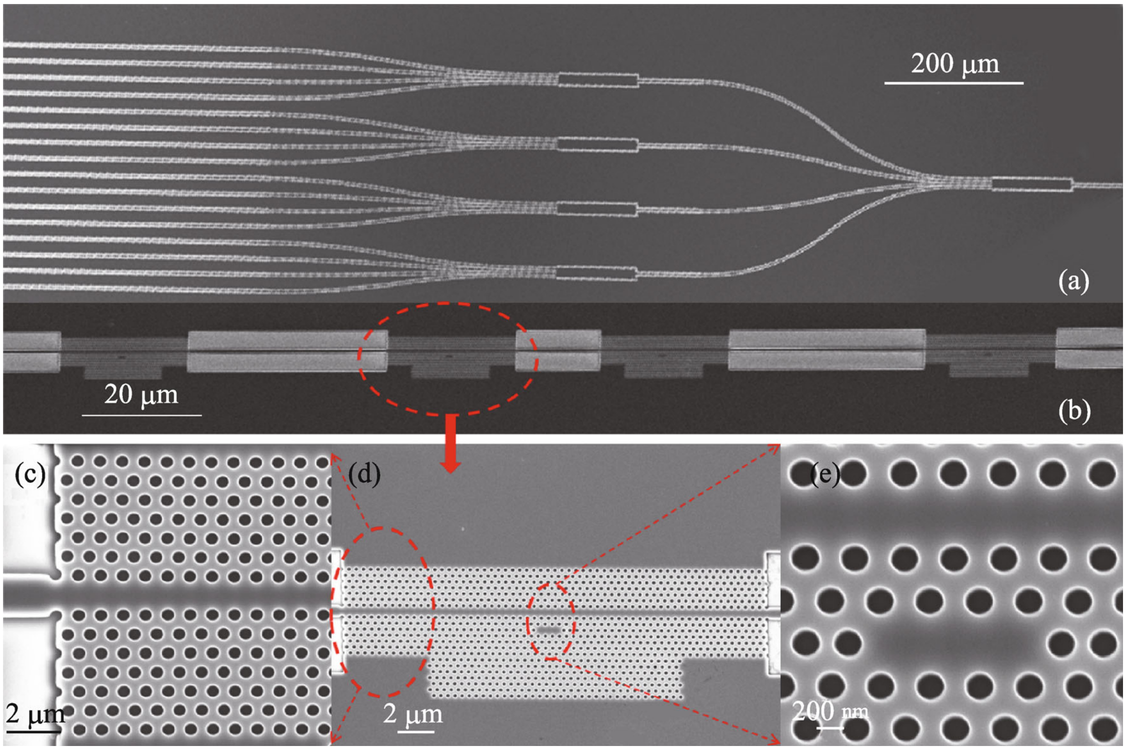

Fig. 15 Scanning electron micrograph of the fabricated device. (a) Full device with 16 arms; (b) each of the 16 arms with 4 cascaded microcavities; (c) PCW adiabatic group index taper achieved by adiabatic width taper of PCW and high group index region; (d) one of the 4 cascaded microcavities shown in (b); (e) close up of the L3 PCM located 2 rows away from a W1 PCW [49]

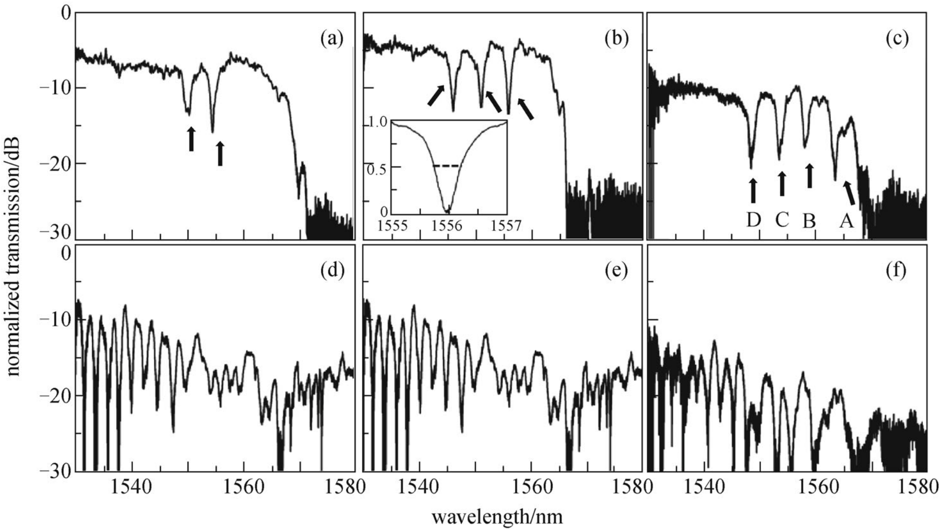

Fig. 16 Normalized transmission spectral of W1 PCW with coupled series-connected L3 PCMs. (a) 2 cavities, (b) 3 cavities and (c) 4 cavities with index taper; (d) 2 cavities, (e) 3 cavities and (f) 4 cavities without index taper. All spectra are measured in water ambient. Resonant peaks are shown by arrows in (a), (b) and (c). In (c), resonant peaks are also labeled as A, B, C and D corresponding to Fig. 14. Inset (b) shows magnified linear scale spectrum of resonance peak closest to the bandedge. The dash line shows the full width at half maximum (FWHM) [49]

this PCM is coupled to the PCW at the ridge waveguide-PCW interface at n_g~ 6 instead of n_g~13 which is in the absence of a group index taper.

Since the wavelengths C, B and A that are dropped in succeeding PC stages must first propagate through the PC stage with a = 392.5 nm, Fig. 14 shows that in the absence of a group index taper, these wavelengths would be coupled into the first PC stage at increasing group indices, reaching n_g = 34 at the resonance wavelength A. Such a large group index mismatch with the single mode strip waveguide makes the coupling efficiency very low. It also results in huge Fresnel reflections and Fabry-Perot resonance fringes in the output transmission spectra as observed in Figs. 16(d), 16(e) and 16(f). We also note the higher propagation loss with increasing series cascading of PC sections. The higher loss and decrease in extinction ratio is also evidenced by Fig. 16, where a bandedge is vaguely discernible in Fig. 16(d), by comparing with Fig. 16(a); however, no sharp bandedges can be seen in Figs. 16 (e) and 16(f). When a group index taper is employed, resonance wavelength A instead couples to the first PC pattern and succeeding PC patterns at a low group index n_g = 7.5 which significantly lowers the reflection losses and Fabry-Perot fringes. Noise ripples arising from such reflection is thus suppressed below 2 dB. The transmission bandedge is clearly observable in each case. The dispersion engineering is done in each stage, so that the resonance wavelength A dropped in the PCM in the last (fourth) stage with a = 396 nm has significantly reduced reflection losses in preceding stages. The same argument holds for resonances C and B dropped by the L3 microcavities in the second and third PC stages in series.

The series cascaded PCMs are next combined with two-stage cascaded 1 × 4 MMIs to build a high density microarray with 1 input arm and 16 output arms, as shown in Fig. 15(a). 4 PCMs are connected in series on each arm. Thus, in total, 64 (4 × 4 × 4) PCMs are integrated in one device. The output transmission spectrum in all 16 arms (4×4) is shown in Fig. 17. All 16 arms have similar spectra; 4 distinct resonant peaks and sharp bandedges can be seen from each spectrum. The Q-factor in all microcavities in water varies between 2000 and 4000, which is a typical range of Q's that have been observed in our oxide clad single L3 PCMs in silicon. The location of the resonant peaks and bandedges are very similar. Small differences in absolute wavelength are observed due to fabrication imperfections. In biosensing, or chemical sensing, such small differences in the absolute wavelength do not matter since the relative resonance wavelength shift is the parameter of interest.

5 Commercial foundry fabrication of 2D photonic crystal devices

The 2D PC devices studied in research were later translated to fabrication in a commercial foundry. Figures 18(a) and 18(b) show SEM images of two typical devices, that were fabricated in Rpizfab, Ghent, Belgium. Figures 18(c) and 18(d) show the resonance spectra corresponding to the devices in Figs. 18(a) and 18(b) respectively. Several devices were fabricated on a chip as shown in Fig. 19, at a much higher density than possible in ebeam-lithography-fabricated silicon PC chips in university cleanrooms. As

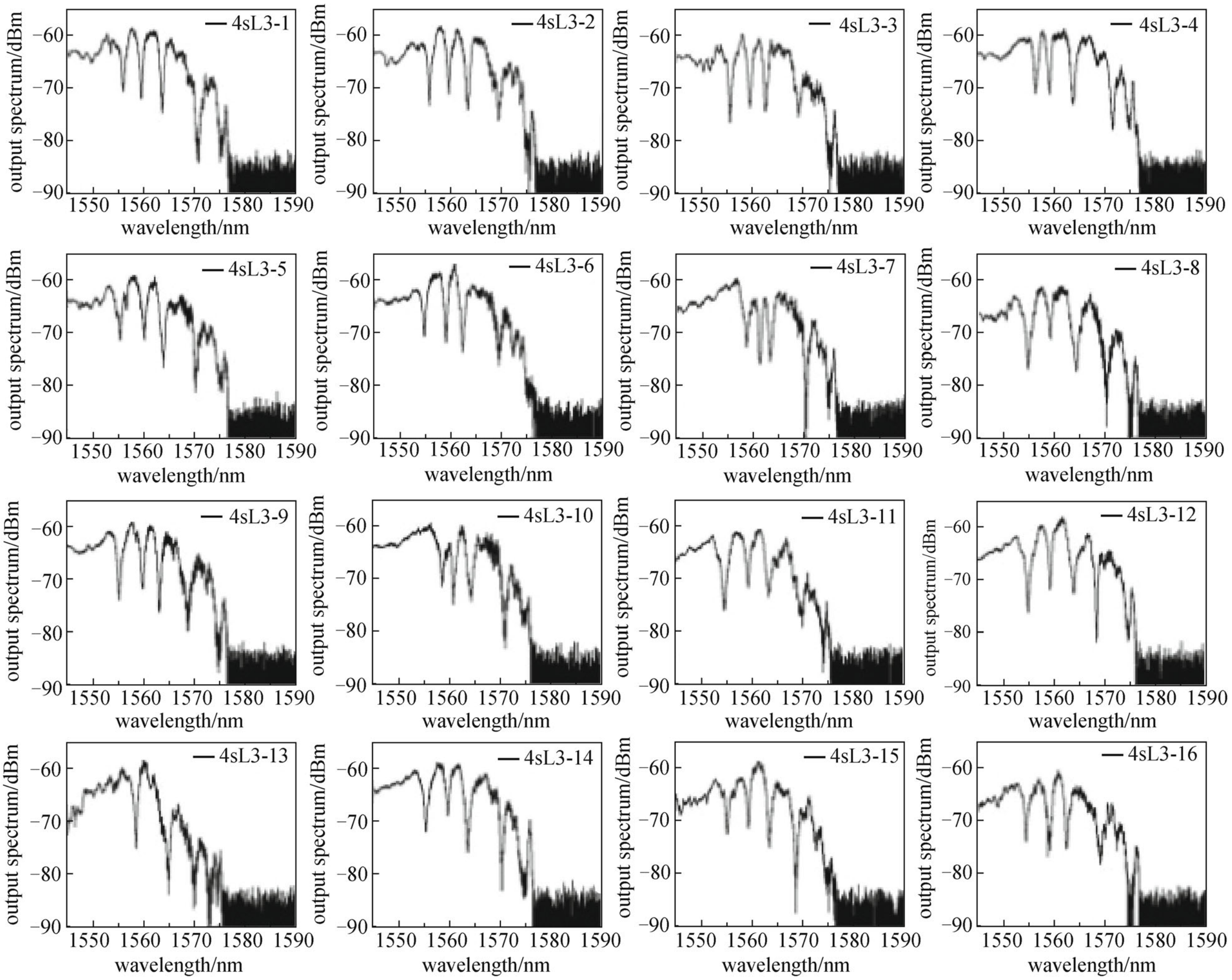

Fig. 17 Output spectra of high density microarray with a total of 64 sensors integrated into 16 arms inside one device. 4 series-connected L3 microcavity are side coupled to PCW on each arm. All spectra are measured in water. 16 arms are made from a two stage cascaded 1 × 4 MMI in Fig. 15(a) [49]

can be seen, by direct comparison with similar devices fabricated at the university research laboratories, the devices fabricated by Epixfab have typical *Q* factors ~40000 compared to typical values ~10000 observed in our university fabricated devices, when measured in water.

6 Sensing of biomarkers for various applications on chip

6.1 Chip-integrated detection of lung cancer cell line lysates

We experimentally demonstrated label-free PCM biosensors in SOI to detect the epithelial-mesenchymal transition (EMT) transcription factor, ZEB1, in minute volumes of sample. Multiplexed specific detection of ZEB1 in lysates from NCI-H358 lung cancer cells down to an estimated concentration of 2 cells per micro-liter was demonstrated. L13 PCMs, coupled to W1 PCWs, are employed in which resonances show high *Q* in the bio-ambient PBS. When the sensor surface is derivatized with a specific antibody, the binding of the corresponding antigen from a complex whole-cell lysate generates a change in refractive index in the vicinity of the PCM, leading to a change in the resonance wavelength of the resonance modes of the PCM. The shift in the resonance wavelength reveals the presence of the antigen. Multiplexed sensors permit simultaneous detection of many binding interactions with specific immobilized antibodies from the same bio-sample at the same instant of time. Specificity was demonstrated using a sandwich assay which further amplifies the detection sensitivity at low concentrations. The device representeda proof-of-concept demonstration of label-free, high throughput, multiplexed detection of cancer cells with specificity and sensitivity on a silicon chip platform, using sandwiched assay techniques. Details are covered in Ref. [50].

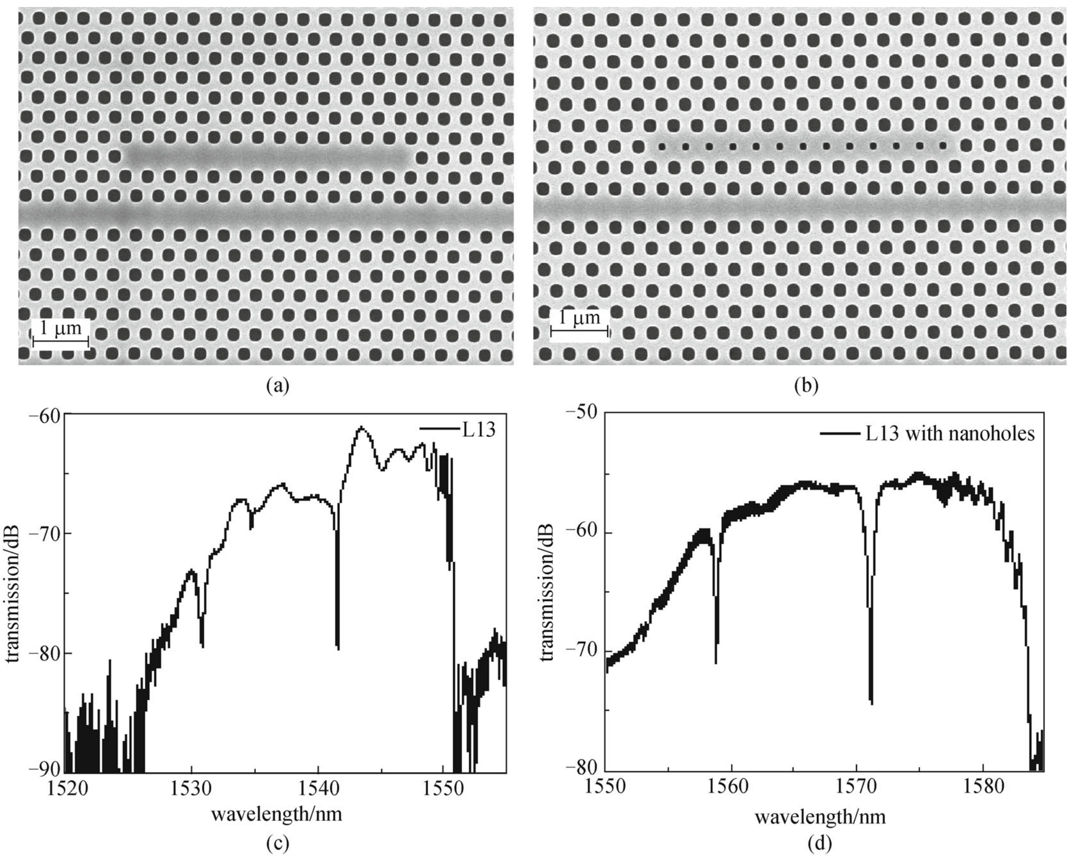

Fig. 18 SEM images of (a) L13 and (b) L13 with nanoholes devices and their respective transmission spectra in (c) and (d), from devices fabricated in a commercial foundry [51]

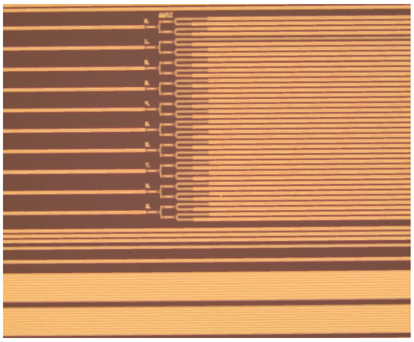

Fig. 19 Dense arrays of devices on a chip multiplexed with MMIs [51]

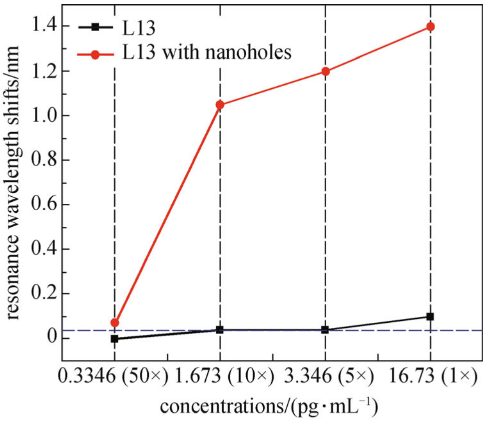

Fig. 20 Plot showing the enhanced sensitivity of L13 with nanohole type of PCM versus conventional L13 PCM, with respect to detection of pancreatic cancer biomarkers [51]

6.2 Chip-integrated detection of pancreatic cancer biomarkers

2D PCMs were fabricated by photolithography and their respective sensitivities to biomarkers in patient serum samples were compared for different microcavity characteristics of quality factor and analyte fill fraction. Three different biomarkers in plasma from pancreatic cancer patients were experimentally detected by conventional L13 PCMs without nanoholes and higher sensitivity L13 PCMs with nanoholes. 8.8 femto-molar (0.334 pg/mL) concentration of pancreatic cancer biomarker in patient plasma samples was experimentally detected at 50 times dilution than ELISA in a PCM with high quality factor and high analyte fill fraction, as shown in Fig. 20. A higher sensitivity was observed, as expected with a L13 PCM with nanoholes versus the L13 PCM without nanoholes due to the higher overlap integral in the former (Fig. 20). Details are covered in Ref. [51].

6.3 Chip-integrated detection of antibiotics for therapeutic drug monitoring

PCM sensors on SOI substrates were utilized as on-chip biosensors to detect small molecule antibiotics with high specificity. Three types of antibiotics, with molecular weight 467.5, 477.6, and 1449.3 g/mol were successfully detected when they bound to their specific conjugate antibodies pre-immobilized on the sensor surface. Wide dynamic detection range of antibiotics gentamicin over 6 orders of magnitude in concentration (from 100 pg/mL to over 10 μg/mL) was realized on a single silicon sensor chip by combining four distinct types of PC biosensors with different biomarker concentration detection limits [52].

6.4 Chip-integrated detection of heavy metals in water

Heavy metal ions released into theenvironment from industrial processes lead to various health hazards. We demonstrated an on-chip label-free detection approach that allows high-sensitivity and high-throughput detection of heavy metals. 2D PCMs were combined by MMI to form a sensor array. We experimentally demonstrated the detection of cadmium-chelate conjugate with concentration as low as 5 parts-per-billion (ppb) [53].

7 Conclusions

Silicon based chip integrated PC biosensors have demonstrated very high sensitivities till date versus competing photonic biosensor technologies. We have investigated the design methods to achieve high sensitivities and minimum detection limits as a function of cavity resonant mode quality factor, fill fraction and the group velocity of the waveguide at the resonant frequency of the microcavity. With judiciously chosen designs, we investigated applications in the sensing of biomarkers for lung cancer and pancreatic cancer, in antibiotic detection for therapeutic drug monitoring, and heavy metal sensing in water pollution monitoring.

Acknowledgements The review of our research presented here has been sponsored by various contracts and grants, namely National Cancer Institute SBIR Contracts # HHSN261201000085C, #HHSN261201200043C, US Army SBIR Contract #W911SR-12-C-0046, NSF Grant # # IIP-1127251 and DOE SBIR Grant #DE-SC0013177.

References

1. Engvall E, Perlmann P. Enzyme-linked immunosorbent assay (ELISA) quantitative assay of immunoglobulin G. Immunochemistry, 1971, 8(9): 871–874
2. Towbin H, Staehelin T, Gordon J. Electrophoretic transfer of proteins from polyacrylamide gels to nitrocellulose sheets: procedure and some applications. Proceedings of the National Academy of Sciences of the United States of America, 1979, 76(9): 4350–4354
3. Kevil C G, Walsh L, Laroux F S, Kalogeris T, Grisham M B, Alexander J S. An Improved, Rapid Northern Protocol. Biochemical & Biophysical Research Communications, 1977, 238(2): 277–279
4. Ren H C, Vollmer F, Arnold S, Libchaber A. High-*Q* microsphere biosensor-analysis for adsorption of rodlike bacteria. Optics Express, 2007, 15(25): 17410–17423
5. Šípová H, Zhang S, Dudley A M, Galas D, Wang K, Homola J. Surface plasmon resonance biosensor for rapid label-free detection of microribonucleic acid at subfemtomole level. Analytical Chemistry, 2010, 82(24): 10110–10115
6. Densmore A, Vachon M, Xu D X, Janz S, Ma R, Li Y H, Lopinski G, Delâge A, Lapointe J, Luebbert C C, Liu Q Y, Cheben P, Schmid J H. Silicon photonic wire biosensor array for multiplexed real-time and label-free molecular detection. Optics Letters, 2009, 34(23): 3598–3600
7. Luff B J, Wilkinson J S, Piehler J, Hollenbach U, Ingenhoff J, Fabricius N. Integrated optical Mach-Zehnder biosensor. Journal of Lightwave Technology, 1998, 16(4): 583–592
8. Fang Y, Ferrie A M, Fontaine N H, Mauro J, Balakrishnan J. Resonant waveguide grating biosensor for living cell sensing. Biophysical Journal, 2006, 91(5): 1925–1940
9. Iqbal M, Gleeson M A, Spaugh B, Tybor F, Gunn W G, Hochberg M, Baehr-Jones T, Bailey R C, Gunn L C. Label-free biosensor arrays based on silicon ring resonators and high-speed optical scanning instrumentation. IEEE Journal of Selected Topics in Quantum Electronics, 2010, 16(3): 654–661
10. Kang C, Phare C T, Vlasov Y A, Assefa S, Weiss S M. Photonic crystal slab sensor with enhanced surface area. Optics Express, 2010, 18(26): 27930–27937
11. Block I D, Chan L L, Cunningham B T. Photonic crystal optical biosensor incorporating structured low-index porous dielectric. Sensors and Actuators. B, Chemical, 2006, 120(1): 187–193
12. Skivesen N, Têtu A, Kristensen M, Kjems J, Frandsen L H, Borel P I. Photonic-crystal waveguide biosensor. Optics Express, 2007, 15 (6): 3169–3176
13. Vashist S K, Luppa P B, Yeo L Y, Ozcan A, Luong J H T. Emerging technologies for next-generation point-of-care testing. Trends in Biotechnology, 2015, 33(11): 692–705
14. Liang P S, Park T S, Yoon J Y. Rapid and reagentless detection of microbial contamination within meat utilizing a smartphone-based biosensor. Scientific Reports, 2014, 4(5953): 5953
15. Chakravarty S, Topol'ancik J, Bhattacharya P, Chakrabarti S, Kang Y, Meyerhoff M E. Ion detection with photonic crystal microcavities. Optics Letters, 2005, 30(19): 2578–2580
16. Lee M R, Fauchet P M. Two-dimensional silicon photonic crystal based biosensing platform for protein detection. Optics Express, 2007, 15(8): 4530–4535
17. Song B S, Noda S, Asano T, Akahane Y. Ultra-high-*Q* photonic double heterostructure nanocavity. Nature Materials, 2005, 4(3): 207–210

18. Tan C P, Cipriany B R, Lin D M, Craighead H G. Nanoscale resolution, multicomponent biomolecular arrays generated by aligned printing with parylene peel-off. Nano Letters, 2010, 10(2): 719–725
19. Akahane Y, Asano T, Song B S, Noda S. High-*Q* photonic nanocavity in a two-dimensional photonic crystal. Nature, 2003, 425 (6961): 944–947
20. Lin C Y, Wang X, Chakravarty S, Lee B S, Lai W C, Chen R T. Wideband group velocity independent coupling into slow light silicon photonic crystal waveguide. Applied Physics Letters, 2010, 97(18): 183302
21. Lai W C, Chakravarty S, Zou Y, Chen R T. Silicon nano-membrane based photonic crystal microcavities for high sensitivity biosensing. Optics Letters, 2012, 37(7): 1208–1210
22. Chakravarty S, Zou Y, Lai W C, Chen R T. Slow light engineering for high *Q* high sensitivity photonic crystal microcavity biosensors in silicon. Biosensors & Bioelectronics, 2012, 38(1): 170–176
23. Zou Y, Chakravarty S, Kwong D N, Lai W C, Xu X, Lin X, Hosseini A, Chen R T. Cavity-waveguide coupling engineered high sensitivity silicon photonic crystal microcavity biosensors with high yield. IEEE Journal of Selected Topics in Quantum Electronics, 2014, 20(4): 6900710
24. Lai W C, Chakravarty S, Zou Y, Guo Y, Chen R T. Slow light enhanced sensitivity of resonance modes in photonic crystal biosensors. Applied Physics Letters, 2013, 102(4): 041111
25. Mortensen N A, Xiao S, Pedersen J. Liquid-infiltrated photonic crystals-enhanced light-matter interactions for lab-on-achip applications. Microfluidics & Nanofluidics, 2008, 4: 117
26. Chakravarty S, Hosseini A, Xu X, Zhu L, Zou Y, Chen R T. Analysis of ultra-high sensitivity configuration in chip-integrated photonic crystal microcavity bio-sensors Applied Physics Letters, 2014, 104(19): 191109
27. Mehta K K, Orcutt J S, Ram R J. Fano line shapes in transmission spectra of silicon photonic crystal resonators. Applied Physics Letters, 2013, 102(8): 081109
28. White I M, Fan X. On the performance quantification of resonant refractive index sensors. Optics Express, 2008, 16(2): 1020–1028
29. Lai W C, Chakravarty S, Wang X, Lin C Y, Chen R T. Photonic crystal slot waveguide absorption spectrometer for on-chip near-infrared spectroscopy of xylene in water. Applied Physics Letters, 2011, 98(2): 023304
30. McMahon R J, Avidin-Biotin Interactions: Methods and Applications. Berlin: Humana Press, 2008, 90
31. Rahimi S, Hosseini A, Xu X, Subbaraman H, Chen R T. Group-index independent coupling to band engineered SOI photonic crystal waveguide with large slow-down factor. Optics Express, 2011, 19(22): 21832–21841
32. Nagahara K, Morifuji M, Kondow M. Optical coupling between a cavity mode and a waveguide in a two-dimensional photonic crystal. Photonics and Nanostructures- Fundamentals and Applications, 2011, 9(9): 261–268
33. Subramanian A, Kennel S J, Oden P I, Jacobson K B, Woodward J, Doktycz M J. Comparisons of techniques for enzyme immobilization on silicon supports. Enzyme and Microbial Technology, 1999, 24(1-2): 26–34
34. Nelson D L, Cox M M. Lehninger Principles of Biochemistry. 5th ed. New York: W. H. Freeman Macmillan, 2008
35. de Feijter J A, Benjamins J, Veer F A. Ellipsometry as a tool to study the adsorption behavior of synthetic and biopolymers at the air–water interface. Biopolymers, 1978, 17(7): 1759–1772
36. Kuo S C, Lauffenburger D A. Relationship between receptor/ligand binding affinity and adhesion strength. Biophysical Journal, 1993, 65(5): 2191–2200
37. de Groote D, Marchant A, Fauchet F, Jadoul M, Dehart I, Gérard C, Gevaert Y, Lopez M, Gathy R, Franssen J D, Radoux D, Franchimont P J. Characterisation of monoclonal antibodies against human interleukin-10 and their use in an ELISA for the measurement of this cytokine. Journal of Immunological Methods, 1994, 177(1-2): 225–234
38. Scullion M G, Di Falco A, Krauss T F. Slotted photonic crystal cavities with integrated microfluidics for biosensing applications. Biosensors and Bioelectronics, 2011, 27(1): 101–105
39. Li H, Fan X. Characterization of sensing capability of optofluidic ring resonator biosensors. Applied Physics Letters, 2010, 97(1): 011105
40. Barrios C A. Optical slot-waveguide based biochemical sensors. Sensors (Basel, Switzerland), 2009, 9(6): 4751–4765
41. de Vos K, Bartolozzi I, Schacht E, Bienstman P, Baets R. Silicon-on-Insulator microring resonator for sensitive and label-free biosensing. Optics Express, 2007, 15(12): 7610–7615
42. Carlborg C F, Gylfason K B, Kaźmierczak A, Dortu F, Bañuls Polo M J, Maquieira Catala A, Kresbach G M, Sohlström H, Moh T, Vivien L, Popplewell J, Ronan G, Barrios C A, Stemme G, van der Wijngaart W. A packaged optical slot-waveguide ring resonator sensor array for multiplex label-free assays in labs-on-chips. Lab on a Chip, 2010, 10(3): 281–290
43. Dorfner D, Zabel T, Hurlimann T, Hauke N, Frandsen L, Rant U, Abstreiter G, Finley J. Photonic crystal nanostructures for optical biosensing applications. Biosensors and Bioelectronics, 2009, 24 (12): 3688–3692
44. Mandal S, Erickson D. Nanoscale optofluidic sensor arrays. Optics Express, 2008, 16(3): 1623–1631
45. Zlatanovic S, Mirkarimi L W, Sigalas M M, Bynum M A, Chow E, Robotti K M, Burr G W, Esener S, Grot A. Photonic crystal microcavity sensor for ultracompact monitoring of reaction kinetics and protein concentration. Sensors and Actuators. B, Chemical, 2009, 141(1): 13–19
46. Zou Y, Chakravarty S, Lai W C, Lin C Y, Chen R T. Methods to array photonic crystal microcavities for high throughput high sensitivity biosensing on a silicon-chip based platform. Lab on a Chip, 2012, 12(13): 2309–2312
47. Guillermain E, Fauchet P M. Resonant microcavities coupled to a photonic crystal waveguide for multichannel biodetection. Materials Research Society Symposium Proceedings, 2009, 1191
48. Pottier P, Gnan M, De La Rue R M. Efficient coupling into slow-light photonic crystal channel guides using photonic crystal tapers. Optics Express, 2007, 15(11): 6569–6575
49. Zou Y, Chakravarty S, Zhu L, Chen R T. The role of group index engineering in series-connected photonic crystal microcavities for high density sensor microarrays. Applied Physics Letters, 2014, 104 (14): 141103
50. Chakravarty S, Lai W C, Zou Y, Drabkin H A, Gemmill R M,

Simon G R, Chin S H, Chen R T. Multiplexed specific label-free detection of NCI-H358 lung cancer cell line lysates with silicon based photonic crystal microcavity biosensors. Biosensors & Bioelectronics, 2013, 43: 50–55

51. Yang C J, Tang N, Yan H, Chakravarty S, Li D, Chen R T. 193 nm lithography fabricated high sensitivity photonic crystal microcavity biosensors for plasma protein detection in patients with pancreatic cancer. In: Proceedings of CLEO (Optical Society of America), San Jose, CA. 2015, STu4K.5
52. Yan H, Yang C J, Zou Y, Tang N, Chakravarty S, Chen R T. Wide dynamic range specific detection of therapeutic drugs by photonic crystal microcavity arrays. In: Proceedings of CLEO (Optical Society of America), San Jose, CA. 2015, STu4K.2
53. Yan H, Tang N, Chakravarty S, Blake DA, Chen RT. High-sensitivity high-throughput chip based biosensor array for multiplexed detection of heavy metals. 2016, submitted

Swapnajit Chakravarty received his Ph.D. degree in electrical and computer engineering from the University of Michigan, Ann Arbor in 2007. Previously, he obtained his B.E. degree in electrical engineering in 2001 from Jadavpur University, Kolkata, India, and his M.S. degree in electrical engineering (electronic materials and devices) from the University of Cincinnati in 2003. Dr. Chakravarty has been an active researcher in PC devices in both III-V and Si. His research area in III-V includes electrically and optically injected 2D PC lasers and light emitting arrays and PC sensors. His recent research interest is to utilize PC slot waveguide devices and PCM devices for lab-on-chip optical sensing and lab-on-chip slow light enhanced optical spectroscopy on silicon platforms in near-infrared and mid-infrared wavelengths, and their integration with near-infrared diode lasers and mid-infrared quantum cascade lasers. Dr. Chakravarty has over 80 publications in refereed journals and conferences. Till date, his research has been supported by multiple SBIR and STTR contracts and grants from NSF, EPA, DoD, DOE and NIH. His research on electrically injected 2D quantum dot PC light emitting arrays received critical acclaim with the Raith Micrograph Award in 2006. In 2013, Dr. Chakravarty was promoted to Senior Member in SPIE and IEEE.

Xiangning Chen is an associate professor at Nanjing University, China. He received his Ph.D. degree from Southeast University, China in 2001. He joined Nanjing University after he finished his post-doctoral research at Tsinghua University in 2003. He worked at the University of Texas at Austin as a visiting scholar from November 2014 to January 2016, on mechanical design related to automating the operation of the biosensing system. He has applied for over 30 patents and published more than 30 papers on electro-mechanical design, software engineering and embedded system. His current research interests include wireless communications, acoustic communications, cloud computing and the internet of things.

Naimei Tang received her Ph.D. degree in biochemistry from Dalian and Beijing Medical University, China in 1996. She has been involved in cancer research for more than 15 years with the interest in cancer biomarker discovery, autoimmune phenomena and signal transduction mechanisms in cancer. She has participated in the biomarker discovery of breast cancer project using T7 phage display system and also involved in the two biomarkers, soluble mesothelin related peptides (SMRP) and osteopontin (OPN) for the diagnosis of mesothelioma study. Recently, she identified 29 tumor associated antigens (TAAs) derived from side population (SP) cells in malignant pleural of mesothelioma with the supporting of the U.S. Environmental Protection Agency. Her current research involves integration of biomarkers for cancers and infectious diseases with the silicon photonic crystal biosensing platform.

Wei-Cheng Lai received his Ph.D. degree in electrical and computer engineering in 2013 from the University of Texas at Austin, Austin. Currently he is a postdoctoral research scientist at the University of California Davis working on silicon photonics.

Yi Zou received his Ph.D. degree in electrical and computer engineering in 2014 from the University of Texas at Austin, Austin. Currently he is a research associate professor in College of Engineering and Applied Sciences in Nanjing University, Nanjing. His research interests include silicon photonics, photonic sensor, mid Infrared photonics and fiber optics.

Hai Yan received his B.S. degree in optical engineering from Huazhong University of Science and Technology, Wuhan, China, in 2010 and M.S. degree in electronic engineering from Tsinghua University, Beijing, China, in 2013. He is currently working towards his Ph.D. degree at the University of Texas at Austin, TX, USA. His research interests include silicon photonic devices for biosensing and optical interconnects applications.

Ray T. Chen is the Keys and Joan Curry/Cullen Trust Endowed Chair Professor. He received his B.S. degree in physics in 1980 from Tsinghua University, his M.S. degree in physics in 1983, and his Ph.D. degree in electrical engineering in 1988, both from the University of California. Chen served as the CTO, Founder, and Chairman of the Board of Radiant Research, Inc. from 2000 to 2001, where he raised 18 million dollars A-Round funding to commercialize polymer-based photonic devices involving over twenty patents, which were acquired by Finisar in 2002, a publicly traded company in the Silicon Valley (NASDAQ:FNSR). He also serves as the founder and Chairman of the Board of Omega Optics Inc. since its initiation in 2001.

His research work has been awarded with over 120 research grants with 800 published papers. He holds 30 issued patents. Chen is a Fellow of IEEE, OSA, and SPIE. He received many awards including the 2008 IEEE Teaching Award, and the 2010 IEEE HKN Loudest Professor Award, 2013 NASA Certified Technical Achievement Award for phased array antenna for moon surveillance. His research has also been recognized as one of the top 10 most promising photonics technologies for commercialization by the International Society of Optical Engineering (SPIE) in 2013. 46 Ph.D. students graduated from his group at UT and many of them are currently professors in the US major research universities.